processes

MDPI

Article

Study on Non-Spherical Deformation Velocity of a Single Cavitation Bubble

Qingmiao Ding [1], Xiaoman Li [2], Yanyu Cui [1,*], Junda Lv [3], Yunlong Shan [1] and Yongqiang Liu [4]

[1] Aeronautical Engineering Institute, Civil Aviation University of China, Tianjin 300300, China; qmding@cauc.edu.cn (Q.D.); shan18822286156@163.com (Y.S.)
[2] Transportation Science and Engineering Institute, Civil Aviation University of China, Tianjin 300300, China; lxmchh@outlook.com
[3] China National Aviation Fuel Supply Co., Ltd., Beijing 100000, China; ljdabc@126.com
[4] School of Energy and Power Engineering, Beihang University, Beijing 100191, China; yoqliu@163.com
* Correspondence: yycui@cauc.edu.cn

Abstract: Cavitation bubbles commonly exist in shipbuilding engineering, ocean engineering, mechanical engineering, chemical industry, and aerospace. Asymmetric deformation of the bubble occurs near the boundary and then has strong destructiveness, such as high amplitude loading. Therefore, the research on non-spherical deformation is of great significance, and the objective of this paper is to investigate the non-spherical collapse dynamics of laser-induced cavitation bubbles when near different boundaries. In this study, experimental data, such as the bubble pulsation process and bubble surface velocity distribution, were obtained by high-speed camera techniques and full-field velocity calculations. Near the different boundaries, the results show that the bubbles appeared to have different collapse shapes, such as near-hemispherical, near-ellipsoidal, near-cone, and near-pea shapes, and the surface velocity distribution is extremely non-uniform. When the bubble near the free surface or rigid boundary collapses, the smaller the stand-off r is, the more obvious the repulsive effect of the free surface or the attractive effect of the rigid boundary is. As the stand-off r decreases, the larger the Bjerknes force and the bubble surface velocity difference and the more pronounced the non-spherical shape becomes.

Keywords: cavitation bubble; free surface; rigid boundary; elastic boundary; non-spherical deformation

Citation: Ding, Q.; Li, X.; Cui, Y.; Lv, J.; Shan, Y.; Liu, Y. Study on Non-Spherical Deformation Velocity of a Single Cavitation Bubble. *Processes* **2024**, *12*, 553. https://doi.org/10.3390/pr12030553

Academic Editor: Sara Liparoti

Received: 3 February 2024
Revised: 4 March 2024
Accepted: 6 March 2024
Published: 12 March 2024

1. Introduction

Cavitation is a physical phenomenon that occurs when the local pressure in a flow field is lower than the corresponding critical pressure. Its presence not only influences the continuity of the fluid, but the violent collapse behavior will also eventually form a high temperature and high-pressure flow field around the cavitation bubble. At this time, the cavitation bubble is also able to move on the microscopic scale of up to hundreds of meters per second, one of the driving sources of liquid flow, and this high-speed liquid flow known as a liquid micro-jet, can impact the boundary and produce up to hundreds of MPa, enough to destroy the majority of the material surface of the water-hammer pressure. In addition, during the collapse phase, the bubble appears to deform asymmetrically and is attracted to the boundary, resulting in a decrease in the distance, which increases the destructive capacity of the micro-jet or other possible destructive behaviors [1–3]. More importantly, the generation of micro-jet is mainly associated with the non-spherical deformation of the cavitation bubble, so it is crucial to study the non-spherical deformation velocity. The boundary, external force, pressure gradient, and other factors can make the shape of the cavitation bubble become an asymmetric structure [4]. In general, non-spherical cavitation bubbles are highly destructive, causing a high amplitude loading at nearby boundaries [5].

The asymmetric collapse of cavitation bubbles often occurs near the boundaries, and micro-jets are formed. The physical properties of the boundaries are crucial for the bubble,

especially asymmetric deformation [6]. The study of bubbles near a single boundary comprises studies mainly of near the free surface, elastic boundary, and rigid boundary. When the bubble grows near the free surface, the surface is pushed upward as the bubble expands, and a substantial water dome is formed, which then evolves into a spike after the bubble shrinks. A high-velocity liquid jet is formed during the collapse phase of the bubble, which penetrates the lower surface of the bubble and starts to expand after reaching a minimum volume, forming a water skirt on the free surface [7,8]. Supponen et al. [9] observed the special dynamics inside the bubble during violent deformation near the free surface by using a high-speed camera. The micro-jet takes on an interesting mushroom-cap shape as it advances into the interior of the bubble in a direction away from the free surface, and the effects of bubble interface instability and non-spherical deformation were discussed. Due to the high-speed flow of the liquid and the effect of the boundaries, the cavitation bubbles' non-spherical shapes appear when the liquid in the venturi, hydrofoil, and serpentine channel flows [10–13]. There exists a different degree of cavitation phenomenon; in addition to the cavitation number, Reynolds number, and thermodynamic parameters, which will affect the cavitation intensity and non-stationary behavior, the deformed shape of the cavitation bubble also has a role. Blake, Lauterborn, and Philipp et al. [1,14–16] conducted earlier extensive studies on bubble dynamics near rigid boundaries. Sagar et al. [17] found that when a bubble grows near a horizontal rigid wall, the maximum radial pressure occurs at the top center of the bubble. The final pressure breaks through the bubble interface and forms a micro-jet. Accordingly, the upper surface of the bubble is curved before the first collapse, which grows toward the bottom surface and ends at the first collapse. The jet strikes the bottom surface in a tangential direction and forms a radially outward flow along the ground surface with a maximum velocity impacting the wall without deceleration, producing a high-intensity impact on the bottom surface. Bubble dynamics near elastic boundaries were studied earlier by Gibson, Blake, and Brujan et al. [18–21]. Ma et al. [22] experimentally found that the deformation of the boundary when the bubble grows near an elastic boundary is pronounced and is strong enough to produce an annular flow in the upper part of the bubble, altering the spherical motion of the bubble. For complex boundaries, the combination of rigid boundaries with other types of boundaries leads to more complex bubble behavior [5,23–25]. Bubbles show non-spherical characteristics near different boundaries, which have strong destructiveness, and the surface velocity distribution can characterize the degree of non-sphericality. Therefore, it is crucial to study the bubble's surface velocity distribution near the boundaries.

In the following, the experimental setup and methods are given in Section 2. Section 3 analyzes the process of near-spherical growth of a bubble and non-spherical growth of a bubble near a single boundary and composite interface and discusses the deformation and deformation velocity of the bubble interface. Section 4 summarizes our main conclusions.

2. Experimental Program

2.1. Experimental Setup

The experiment setup is shown in Figure 1, in which we used a laser-induced single cavitation bubble to study the dynamic behavior of the bubble. The phenomenon of non-spherical deformation of the bubble was observed using high-speed photography. Visualization was performed by a high-speed camera, a Phantom VEO mounted with a telephoto camera lens, which enables recordings at 10,860 fps at a full resolution (1280 × 960 pixels) and up to 423,350 fps at reduced resolution. This experimental configuration included 2 μs exposure time with a 50,000 frame rate, a 20 μs time interval and a 81,700 frame rate, a 12.24 μs time interval. The Dawa series we used was a miniaturized lamp-pumped Nd/YAG nanosecond laser, which belongs to the small and medium energy classes, with a fundamental frequency energy output ranging from 100 mJ to 300 mJ and optional SHG, THG, and FHG multiple harmonics. The laser also features adjustable energy attenuators and red-light indicators. We used the Phantom VEO series of high-speed cameras, which incorporates the latest imaging technology in a compact, reliable, and

easy-to-use camera system. The highest frame rate in the VEO series captures images at 13 G pixels per second at a full resolution. The Pixel Fusion mode increases the speed by another 25% at 640 × 480 pixels or less. It also has an excellent native ISO light sensitivity of up to 25,000 (black and white), more than twice that of other VEO series cameras, giving greater freedom in lighting and optics when shooting some challenging subjects. It also comprised an imaging metrics customized 12-bit depth CMOS sensor element and an 18 um pixel size with a global shutter with double correlation sampling. The high-speed camera is synchronized and comprises the following: the use of a pulsed light source, which can achieve 157 lm/W of ultra-high luminous efficiency; a color-rendering index of up to 80 (a color-rendering index of 90 is optional); a new, high-efficiency spotlight system; and with the irradiation of an object on the surface of extremely high and uniform illuminance, an advanced constant-current drive power supply and active heat dissipation system can bring good working stability. A sub-microsecond synchronization/delay time can be perfectly synchronized with a high-speed camera, which is equivalent to a sub-microsecond shutter; thus, movement appearing as flying appears without tail-dragging. The water tank material used for the experiment is a transparent acrylic plate with the size of 100 × 100 × 100 mm^3, which has a larger size space compared to the cavitation bubble; this is to ignore the sidewall effect. We used 1.0.14 Performance Synchronizer to achieve test synchronization for the Dawa laser, high-speed camera, and light source control after connecting the synchronization cables. Detailed information about the relative position of the bubble near the vertical boundary and the free surface in space is shown in Figure 1. We controlled the distance of the cavitation bubble from each boundary by a three-dimensional moving platform with an accuracy of 0.01 mm. Table 1 shows the experimental parameter settings and the maximum equivalent radius of the bubble: R_m = 1.20 mm. For different boundaries, experiments were carried out at r = 1.30, and at this distance, the bubble does not have direct contact with the boundaries but appears with non-spherical deformation. In particular, another experiment at r = 1.15 was carried out near the elastic boundary because, apparently, non-spherical deformation does not occur at r = 1.30, thus shortening the distance.

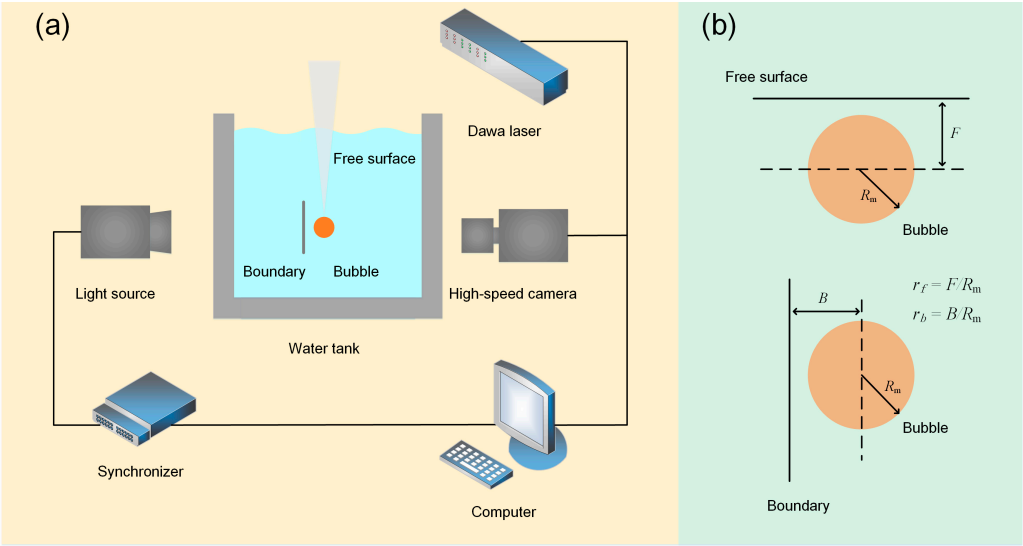

Figure 1. The schematic description for the experimental setup: (**a**) the whole system, and (**b**) the detailed information about the relative position between the bubble and boundary in space.

Table 1. Experimental parameter settings. The maximum equivalent radius of the bubble is R_{m} = 1.20 mm.

Boundary Types	The Distance	Shape of the Collapsing Bubble
none		spherical
free surface	r_f = 1.30	hemispherical
rigid boundary	r_b = 1.30	ellipsoidal
elastic boundary	r_b = 1.30, r_b = 1.15	cone-shaped
free surface and rigid boundary	$r_b = r_f$ = 1.30	pea-shaped

2.2. Full-Field Velocity Calculation

Our velocity processing software is capable of recording velocity distribution information at many spatial points in the same transient. The calculation principle is as follows: In the vicinity of a point where both velocities and velocity gradients are known, the local velocity field can be approximated by a Taylor expansion

$$\begin{bmatrix} u \\ v \\ w \end{bmatrix} = \begin{bmatrix} u_0 \\ v_0 \\ w_0 \end{bmatrix} + \begin{bmatrix} \frac{\partial u}{\partial x} & \frac{\partial u}{\partial y} & \frac{\partial u}{\partial z} \\ \frac{\partial v}{\partial x} & \frac{\partial v}{\partial y} & \frac{\partial v}{\partial z} \\ \frac{\partial w}{\partial x} & \frac{\partial w}{\partial y} & \frac{\partial w}{\partial z} \end{bmatrix} \begin{bmatrix} x - x_0 \\ y - y_0 \\ z - z_0 \end{bmatrix} + o\left(\Delta^2\right) \tag{1}$$

or in a single matrix expression

$$\begin{bmatrix} u \\ v \\ w \end{bmatrix} = \begin{bmatrix} \frac{\partial u}{\partial x} & \frac{\partial u}{\partial y} & \frac{\partial u}{\partial z} & u_0 \\ \frac{\partial v}{\partial x} & \frac{\partial v}{\partial y} & \frac{\partial v}{\partial z} & v_0 \\ \frac{\partial w}{\partial x} & \frac{\partial w}{\partial y} & \frac{\partial w}{\partial z} & w_0 \end{bmatrix} \begin{bmatrix} \Delta x \\ \Delta y \\ \Delta z \\ 1 \end{bmatrix} + o\left(\Delta^2\right) \tag{2}$$

which is an affine transform where the velocities (u_0, v_0, w_0) and all gradients are evaluated in the reference point (x_0, y_0, z_0) and (Δx, Δy, Δz) = ($x - x_0$, $y - y_0$, $z - z_0$).

If we multiply with Δt—the time between the two images—the velocities become displacements, which can be measured in pixels, and if the (x, y, z) positions are also measured in pixels, all the gradients become dimensionless.

In 2D, this simplifies to (omitting higher-order terms):

$$\begin{bmatrix} u \\ v \end{bmatrix} \cong \begin{bmatrix} \frac{\partial u}{\partial x} & \frac{\partial u}{\partial y} & u_0 \\ \frac{\partial v}{\partial x} & \frac{\partial v}{\partial y} & v_0 \end{bmatrix} \begin{bmatrix} \Delta x \\ \Delta y \\ 1 \end{bmatrix} \tag{3}$$

where all (u, v) and their gradients now describe the displacements in pixels, and (Δx, Δy) describes the distances in pixels from the center of the interrogation area, where displacements and gradients apply. Since both (u, v) displacements and (x, y) positions are in pixels, the spatial gradients become pixel/pixel, dimensionless.

The validation is used to prevent outliers from disturbing iterations and, thus, velocity measurements. The validation is conducted by first applying peak validation on the image cross-correlation and secondly by comparing each vector to its neighbors using the universal outlier detection algorithm. To invalidate the vectors based on the image correlation peaks, three peak validation schemes are as follows: if the peak height validation is enabled, then only the correlation peaks above the specified value will be retained as valid; if the peak height validation is enabled, then the ratio between the two highest correlation peaks is calculated. This ratio must be higher than the specified value to validate the calculated displacement. The typical value for the peak height ratio is 1.2, and if the S/N ratio is enabled, first, the noise level in the correlation plane is evaluated by the root mean square of the negative correlation values. If the ratio between the correlation peak height and the noise level is above the specified value, then the calculated displacement is considered valid. We used the peak height validation criteria before performing the computational measurements. The value was set to 0.15, which means that the value is the minimum

accepted value to ensure the accuracy of the results. In addition, universal outlier detection was used to set the acceptance limit to 2.00. In addition, we also compared and analyzed the experimentally measured velocities with the bubble surface velocities computed by the Rayleigh theoretical model to verify the accuracy of the experimental results.

3. Results

3.1. Near-Spherical Collapse of Cavitation Bubble

When $p \leq p_v + p_g - 2\sigma/R$, in the influence of the pressure difference between the inside and outside of the bubble, the bubble expands outward, which promotes its surrounding liquid flow outward in the radial direction. Where p is the liquid pressure on the bubble surface, p_v is the saturated vapor pressure inside the bubble, p_g is the gas partial pressure inside the bubble, R is the radius of the bubble, and σ is the surface tension coefficient of the liquid. Currently, the bubble pressure with the bubble expansion continues to decline until it reaches the static equilibrium pressure after the bubble due to the inertia of the surrounding fluid and continues to expand outward to the maximum bubble radius. After the bubble pressure is lower than the equilibrium pressure of the surrounding medium, $p \geq p_v + p_g - 2\sigma/R$, the bubble begins its contraction process; the liquid around the bubble to the center of the bubble causes a polymerization flow and makes the volume of the bubble continue to shrink. Then, the bubble pressure also gradually increases until it reaches the static equilibrium conditions, and then the bubble, due to the flow of liquid, contracts excessively. When the bubble shrinks to the minimum radius, the bubble completes a complete expansion and contraction process. As shown in Figure 2, the laser-induced single bubble, under the action of the pressure difference between the inside and outside of the bubble, saw the radius of the bubble increase. The pressure inside the bubble gradually converged with the pressure outside the bubble, and the radius of the bubble reached the maximum at 100 μs, at which time the pressure inside and outside the bubble was basically the same. In the time of 0–100 μs, the expansion velocity of the bubble gradually decreased, and the bubble surface velocity was minimized between 100 μs and 120 μs. In the time of 120–220 μs, the radius of the bubble decreased, the pressure inside the bubble increased again, and the bubble collapsed near 220 μs. In addition, it can be seen in Figure 2 that the bubble basically ensured a better spherical shape during expansion and contraction; the force of the bubble was uniform. At this time, the bubble of the free field was only subjected to buoyancy, which can be basically disregarded for the smaller bubble.

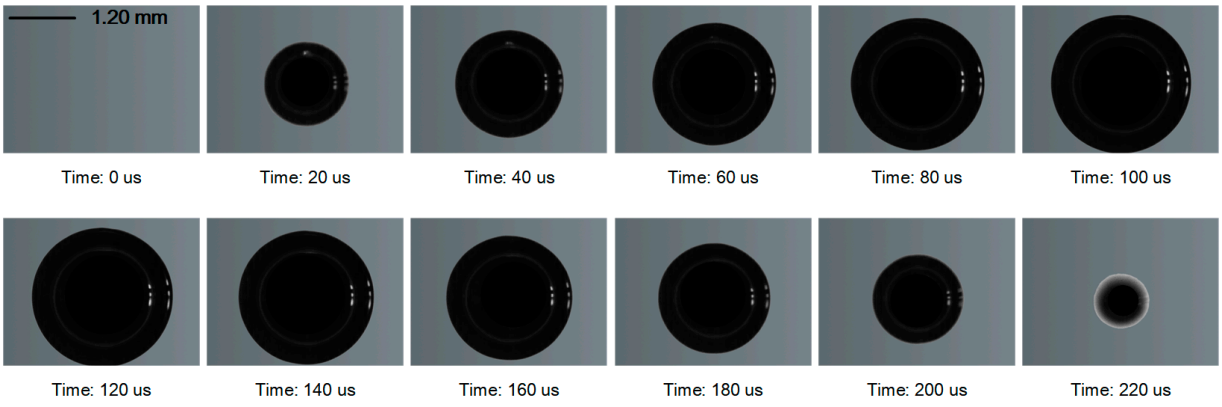

Figure 2. Cavitation bubble dynamics of free field. Time: 0–100 μs, the expanding cavitation bubble. Time: 120–220 μs, the contracting cavitation bubble, R_m = 1.20 mm.

3.2. Non-Spherical Collapse Velocity of Cavitation Bubble near Single Boundary

3.2.1. Near the Free Surface

As shown in Figure 3, when the bubble collapsed near the free surface, distinct non-spherical shapes were observed after 195.84 μs. The bubble expanded during the time 0–110.16 μs, during which the bubble maintained a better spherical shape. The radius of

the bubble reached its maximum at 110.16 μs. The bubble contracted at 122.40–220.32 μs, and the non-spherical shape of the bubble became more and more obvious in the process. At 220.32 μs, a nearly hemispherical shape of the bubble could be observed. The bubble surface velocities were analyzed and calculated, and the results are shown in Figure 4. At 61.20 μs, the expansion velocity of the upper surface of the bubble was larger than that of the lower surface. At 110.16 μs, near the maximum radius, the expansion velocity of the lower surface was larger than that of the upper surface, and at 171.36 μs, the contraction velocity of the upper surface was significantly larger than that of the lower surface. In addition, a special velocity distribution occurred at 110.16 μs, when the bubble expansion velocity was the minimum and at the time junction of expansion and contraction. For the two moments of 61.20 μs and 171.36 μs, the former was the expansion phase, and the latter was the contraction phase, although both showed that the upper surface velocity was larger than the lower surface velocity, and the latter velocity difference was a little larger. The bubble was attracted by the free surface in the expansion phase and repelled in the contraction phase. The cause of the above phenomenon is due to the inhomogeneous distribution of the acting fluid-pressure gradient at the free surface. The asymmetric force on the bubble makes the inward extrusion on the side of the bubble adjacent to the high pressure and the surface of the bubble shrinks at different velocities, respectively, with one side going inward faster than the other. The numerical results for a bubble near the free surface using Eulerian FEM were achieved [8], where the free surface is pushed upwards, and a high-speed liquid jet against the free surface is formed during its collapsing stage. The jet penetrates the lower bubble surface and begins to expand after it reaches its minimum volume, and the water skirt is formed at the free surface during the second expansion of the bubble.

Figure 3. Cavitation bubble dynamics near the free surface. Time: 0–110.16 μs, the expanding cavitation bubble. Time: 122.40–220.32 μs, the contracting cavitation bubble, and apparent non-spherical deformation, r_f = 1.30, R_m = 1.20 mm.

The bubble surface velocity is decomposed along the horizontal and vertical directions, where u is the velocity corresponding to its component in the horizontal direction, and v is the velocity corresponding to its component in the vertical direction. As shown in Figure 5a, $w_{1.30}$ = 5.6 m/s at 171.36 μs due to the uneven force on the bubble. As shown in Figure 5b, the horizontal coordinate represents the stand-off r, which is the ratio of the distance of the bubble from the free surface B to the maximum radius of the bubble R_m. The vertical coordinate represents the difference between the bubble surface velocities in the vertical direction and is dimensionless. The maximum radius of the bubble is in the vicinity of 1.20 mm, at 171.36 μs. From the figure, the bubble surface velocity difference in the vertical direction decreased as the stand-off r increased. The inhomogeneity of the bubble surface velocity in the vertical direction is due to the action of the free surface on the Bjerknes force on the bubble, which tends to decrease with increasing stand-off r. That is, the closer the bubble is to the free surface, the more pronounced the non-spherical shape of the bubble is, and the larger the bubble velocity difference is in the vertical direction.

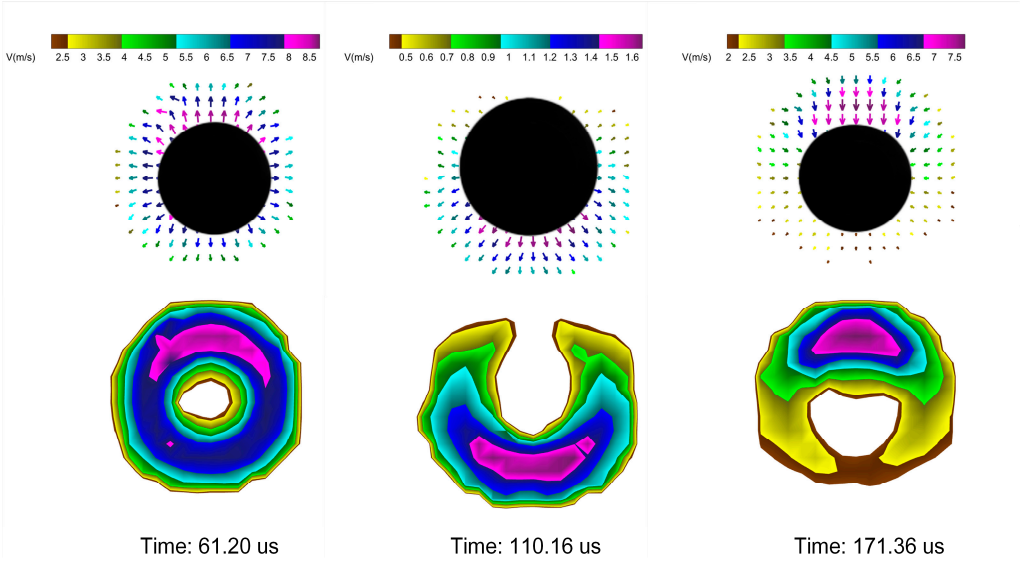

Figure 4. Non-spherical bubble shape due to inhomogeneous bubble surface velocity near the free surface.

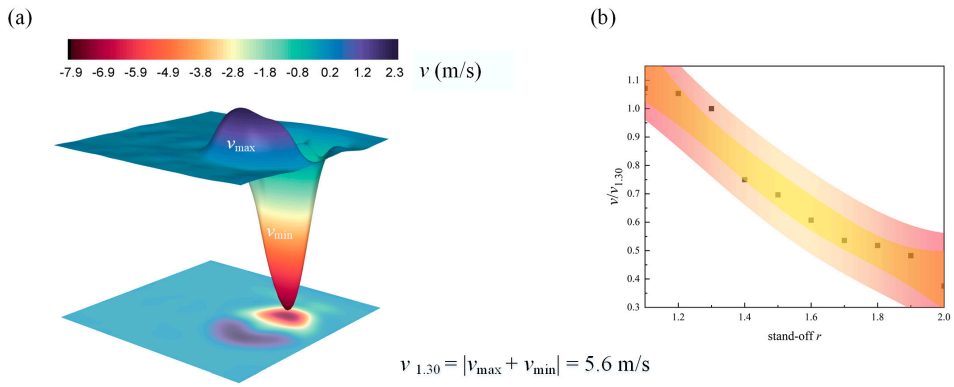

Figure 5. (**a**) Time: 171.36 µs, distribution of decomposition velocity v; (**b**) v velocity difference in bubble surface at a different stand-off r. Among, yellow zone indicate 95% confidence band, red zone indicate 95% prediction band.

3.2.2. Near the Rigid Boundary

During the growth phase, the bubble is approximately spherical; however, during the contraction phase, the irregularities in the velocity and pressure field, together with the presence of the boundary, will be clear in the bubble shape [14]. As shown in Figure 6, the non-spherical shape of the bubble became more and more obvious at the 122.40–220.32 µs contraction phase when the bubble grew near the rigid boundary. The bubble surface velocity distribution is shown in Figure 7. At 61.20 µs, the bubble velocity on the left side was significantly smaller than that on the right side, and there was a low-velocity region near the rigid boundary. At 110.16 µs, the bubble was still in the expansion stage, but at this time, the expansion velocity of the left side was larger than that of the right side, which is the same as that near the free surface, and this time it was at the junction of the expansion and contraction processes. Due to the delay in the flow of fluid between the bubble surface and the boundary, during the collapse phase, the bubble center moves towards the boundary, as the pressure in this region is lower than that of the opposite bubble wall, and this translational motion accelerates during the following collapse phase [1]. At 171.36 µs, the left side was clearly in the low-velocity region, where the contraction velocity was significantly smaller than that of the right side. In the expansion phase, the rigid boundary repelled the bubble, and in the contraction phase, it attracted the bubble. As shown in Figure 8, the horizontal coordinate is the dimensionless distance, and the vertical

coordinate is the velocity difference in the bubble deformation in the horizontal direction. The bubble surface velocity difference in the dimensionless horizontal direction decreased as the stand-off r increased, and the less the non-spherical shape was obvious. Theoretically, as the stand-off r decreased, the Bjerknes gradually increased. According to the Kelvin impulse model and the mirror theory, the equation of the Bjerknes force that was suffered by the bubble near the rigid boundary was gained.

Figure 6. Cavitation bubble dynamics near the rigid boundary. Time: 0–110.16 μs, the expanding cavitation bubble. Time: 122.40–220.32 μs, the contracting cavitation bubble, and apparent non-spherical deformation, r_b = 1.30, R_{m} = 1.20 mm.

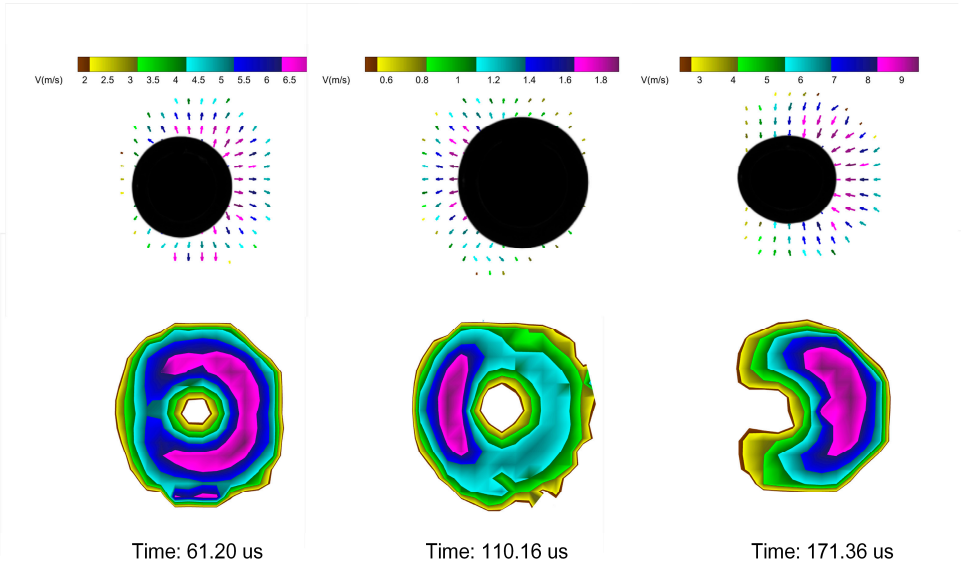

Figure 7. Non-spherical bubble shape due to inhomogeneous bubble surface velocity near the rigid boundary.

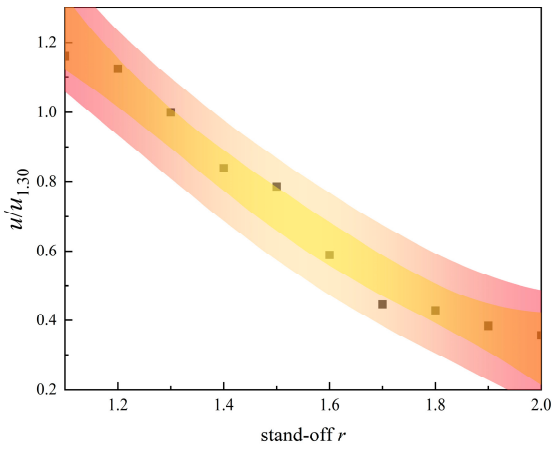

Figure 8. The u velocity difference of bubble surface at different stand-off r. Among, yellow zone indicate 95% confidence band, red zone indicate 95% prediction band.

3.2.3. Near Elastic Boundary

As shown in Figure 9, no obvious non-spherical shapes were observed, r_b = 1.30, when the bubble collapsed near the elastic boundary. When r_b = 1.15, clear non-spherical shapes were observed at 195.84 μs, and the bubble appeared as a conical shape, which is very different from those near the free surface and near the rigid boundary, as shown in Figure 10. The growth and collapse of the cavitation bubble near the elastic boundary, where parts of the bubble surface respond as being near the rigid boundary, whereas in other parts of the bubble surface, the response tends to be near the free surface. The reason for this difference is that during the growth of the bubble, the elastic boundary was deformed convexly and concavely, and this deformation disturbed and altered the flow field between the bubble and the boundary to a certain extent, which, in turn, affected the bubble shape and formed the special shape. The non-spherical shape became more and more obvious at 122.40–220.32 μs. For these two conditions, the bubble surface velocity distribution is shown in Figure 11. At 85.68 μs, the velocity of the right surface was larger than that of the left surface for both. The contraction velocity of the bubble surface close to the elastic boundary was smaller, which is suppressed by the elastic boundary, and the closer the stand-off r was, the more obvious the suppression was, which was basically consistent with that of the bubble in the vicinity of the rigid boundary. In the contraction stage, at r_b = 1.30, the contraction velocity of the left bubble surface was larger than that of the right one, which is different from that near the rigid boundary. This occurred as the elastic boundary appeared convex during the contraction phase of the bubble, which pushed the nearby flow field and increased the contraction velocity of the bubble surface near the elastic boundary. At r_b = 1.15, the velocity of the bubble surface near the elastic boundary was suppressed due to the closer elastic boundary, but the maximum bubble surface contraction velocity occurred at the upper and lower sides near the elastic boundary. Due to the characteristic of the elastic boundary, the bubble surface contraction velocity appeared different. The numerical results for a bubble near the elastic boundary using the fluid-structure interaction model have been carried out [26–28]. Convex and concave deformation of the elastic boundary occurs, and an annular liquid jet is formed during its collapsing stage, which is the reason for the special non-spherical shape.

Figure 9. Cavitation bubble dynamics near the elastic boundary. Time: 0–110.16 μs, the expanding cavitation bubble. Time: 122.40–220.32 μs, the contracting cavitation bubble, r_b = 1.30, R_m = 1.20 mm.

The bubble was influenced by the boundary, and the deformation velocity of the bubble surface was not uniform. During the contraction stage, near the free surface, the maximum bubble surface velocity appeared nearby the free surface; near the rigid boundary, the minimum bubble surface velocity appeared nearby the rigid boundary; near the elastic boundary, due to its characterizations between the free surface and the rigid boundary, the minimum bubble surface velocity appeared nearby the elastic boundary, the maximum bubble surface velocity appeared nearby the elastic boundary on both sides of the bubble. The above phenomenon is due to the bubble experiencing diverse Bjerknes force directions near these three boundaries. Specifically, near the free surface, the bubble is subjected to Bjerknes force that the direction of vertical and back from the free surface. Near the rigid boundary, the bubble is subjected to the Bjerknes force, the direction of vertical and

pointing towards the rigid boundary. Similarly, near the elastic boundary, the Bjerknes force acts in directions both toward and back from the elastic boundary direction. The difference in the direction of the Bjerknes force is that near the free surface and near the elastic boundary, there is a significant deformation of the boundaries, which, in turn, is sufficient to affect the dynamics of the bubble again.

Figure 10. Cavitation bubble dynamics near the elastic boundary. Time: 0–110.16 µs, the expanding cavitation bubble. Time: 122.40–220.32 µs, the contracting cavitation bubble, and apparent non-spherical deformation, r_b = 1.15, R_{m} = 1.20 mm.

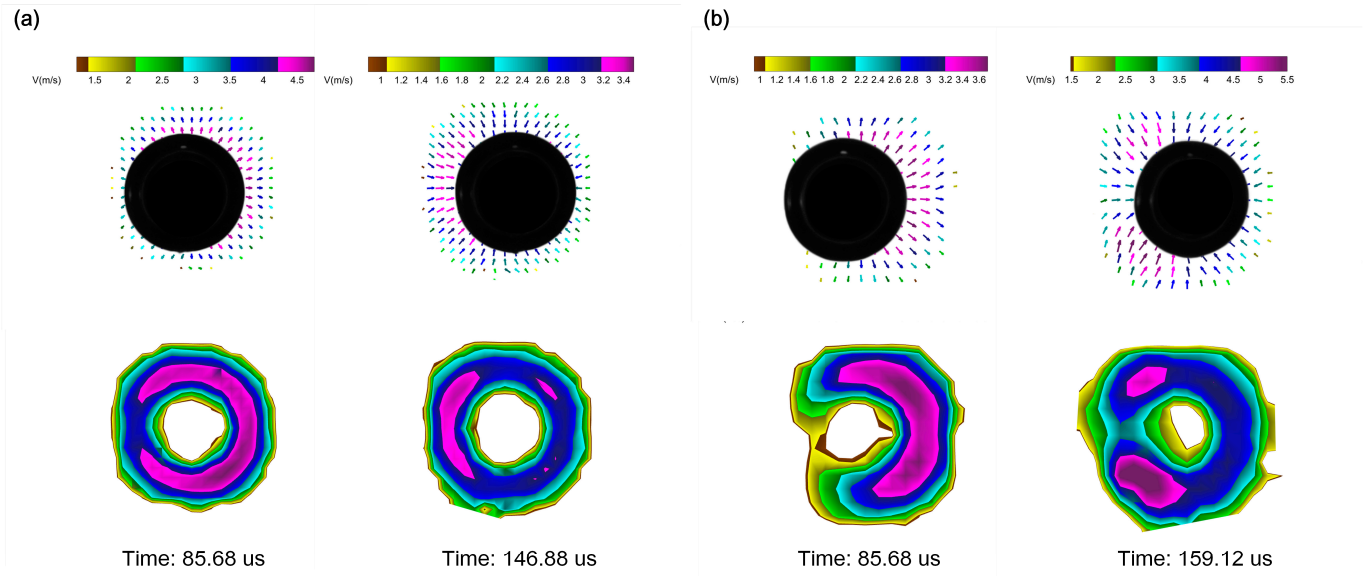

Figure 11. Non-spherical bubble shape due to inhomogeneous bubble surface velocity near the elastic boundary, (**a**) r_b = 1.30 (**b**) r_b = 1.15.

3.3. Non-Spherical Collapse Velocity of Cavitation Bubble near Composite Boundaries

When only the free surface existed, its repulsive action caused the bubble tip to concave downward and appear non-spherical. When only the vertical rigid boundary existed, its attraction caused the bubble surface toward the boundary to be concave and appear non-spherical. When both the rigid boundary and the free surface existed, the combined effect made the bubble's shape distorted, bubble morphology occurred, and its irregularity changed. As shown in Figure 12, when the bubble grew near the rigid boundary and the free surface, a clear non-spherical shape was observed at 208.08 µs, and the spherical shape of the cavitation bubble was severely destabilized, with the tip of the bubble sinking diagonally downward, resulting in the formation of a bubble similar to the shape of a pea. Due to the combined effect of the vertical boundary and the free surface, the location of the maximum bubble surface velocity was non-axisymmetric, deviating from the vertical direction and deflecting towards the vertical wall, as shown in Figure 13. At 61.20 µs and 85.68 µs, the bubble was in the expansion stage, and the position of the maximum bubble surface velocity was at an angle to the vertical direction. At 171.36 µs,

the bubble was in the contraction stage, and the maximum bubble surface velocity position was deflected along a certain angle, and the bubble surface velocity difference was larger at this angle than in the expansion stage. Under this condition, the cavitation bubble was not only subjected to the Bjerknes force in the vertical direction of the free surface but also subjected to the Bjerknes force in the horizontal direction of the rigid boundary, and thus, it was subjected to a combined force deviating from the vertical direction.

Figure 12. Cavitation bubble dynamics near free surface and rigid boundary. Time: 0–110.16 μs, the expanding cavitation bubble. Time: 122.40–220.32 μs, the contracting cavitation bubble, and apparent non-spherical deformation, $r_b = r_f = 1.30$, $R_m = 1.20$ mm.

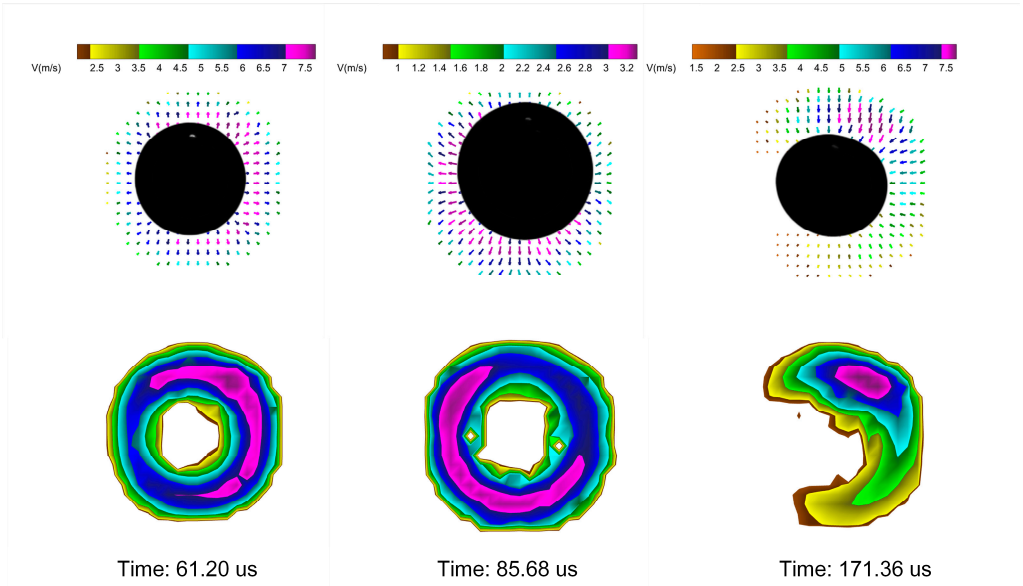

Figure 13. Non-spherical bubble shape due to inhomogeneous bubble surface velocity near the free surface and rigid boundary.

4. Conclusions

The non-spherical deformation of cavitation bubbles is sensitive to boundary types. In this study, the non-spherical deformation behavior of a bubble under multiple types of boundaries was investigated by using high-speed camera techniques and full-field velocity calculations, and the velocity distribution of the bubble surface was analyzed. This provides valuable theoretical guidance for the medical application of cavitation bubbles. In medical therapies using cavitation bubbles, bubbles grow and collapse in and around soft media and biological tissues, and the inappropriate application of the cavitation effect can lead to side effects, such as hemolysis due to the rupture of hemoglobinocytes and hemorrhage due to the rupture of blood vessels. This study of the analysis of bubble surface velocities near different boundaries can guide practical situations to control the appropriate distance and mitigate the side effects of the cavitation effect in medical diagnostic and therapeutic techniques. The main conclusions are as follows:

(1) The bubble collapsed to a near-spherical shape when it was in the free field, but when the bubble was near the boundary, the non-spherical bubble collapse occurred due to the asymmetric force on the bubble. Further, the bubbles collapsed to a near-hemispherical shape near the free surface and to a near-ellipsoidal shape near the rigid boundary. The bubble also collapsed to a near-cone shape near the elastic boundary and a near-pea shape near the free surface and the rigid boundary.

(2) The bubble was influenced by the boundary, and then the deformation velocity of the bubble surface was not uniform. During the contraction stage, near the free surface, the maximum bubble surface velocity appeared nearby the free surface; near the rigid boundary, the minimum bubble surface velocity appeared nearby the rigid boundary; near the elastic boundary, due to its characterizations between the free surface and the rigid boundary, the minimum bubble surface velocity appeared nearby the elastic boundary, the maximum bubble surface velocity appeared nearby the elastic boundary on both sides of the bubble; near the free surface and the rigid boundary, the position of the maximum bubble surface velocity appeared shift. Namely, the free surface promotes bubble surface velocity, the rigid boundary inhibits bubble surface velocity, and the elastic boundary both promotes and inhibits bubble surface velocity.

(3) When the bubble is near the free surface or rigid boundary, the smaller the stand-off r is, the more obvious the repulsive effect of the free surface or the attractive effect of the rigid boundary is. As the stand-off r decreases, the larger the Bjerknes force and the bubble surface velocity difference, and the more pronounced the non-spherical shape.

Author Contributions: Conceptualization, Q.D. and Y.C.; methodology, X.L.; software, J.L.; validation, Y.S. and Y.L.; data curation, Q.D.; writing—original draft preparation, X.L.; writing—review and editing, Q.D. and Y.C.; supervision, Y.C.; funding acquisition, Q.D. All authors have read and agreed to the published version of the manuscript.

Funding: This document is the result of a research project funded by the Ministry of Education Chunhui Project (HZKY20220606-202201390) and the Civil Aviation University of China Postgraduate Scientific Research Innovation Project—Aviation Special Project (2022YJS069).

Data Availability Statement: Data are contained within the article.

Conflicts of Interest: Author Junda Lv was employed by the company China National Aviation Fuel Supply Co., Ltd. The remaining authors declare that the research was conducted in the absence of any commercial or financial relationships that could be construed as a potential conflict of interest.

References

1. Philipp, A.; Lauterborn, W. Cavitation erosion by single laser-produced bubbles. *J. Fluid Mech.* **2000**, *361*, 75–116. [CrossRef]
2. Fabian, R.; Carsten, D.; Claus-Dieter, O. Cavitation erosion by shockwave self-focusing of a single bubble. *Ultrason. Sonochem.* **2022**, *90*, 106131.
3. Brujan, E.A.; Keen, G.S.; Vogel, A.; Blake, J.R. The final stage of the collapse of a cavitation bubble close to a rigid boundary. *Phys. Fluids* **2002**, *14*, 85–92. [CrossRef]
4. Han, S.; Li, Y.; Zhu, H. The similarities and differences between the bubble collapse near a solid wall and in free water. *Eur. J. Mech. B Fluids* **2020**, *84*, 1110. [CrossRef]
5. Kan, X.Y.; Yan, J.L.; Li, S.; Zhang, A.M. Rupture of a rubber sheet by a cavitation bubble: An experimental study. *Acta Mechanica Sinica* **2021**, *37*, 1489–1497. [CrossRef]
6. Zhang, M.A.; Cui, P.; Wang, Y. Experiments on bubble dynamics between a free surface and a rigid wall. *Exp. Fluids Exp. Methods Their Appl. Fluid Flow* **2013**, *54*, 1602. [CrossRef]
7. Huang, G.; Zhang, M.; Ma, X.; Chang, Q.; Zheng, C.; Huang, B. Dynamic behavior of a single bubble between the free surface and rigid wall. *Ultrason. Sonochem.* **2020**, *67*, 105147. [CrossRef]
8. Wang, S.P.; Zhang, A.M.; Liu, Y.L.; Zhang, S.; Cui, P. Bubble dynamics and its applications. *J. Hydrodyn.* **2018**, *30*, 975–991. [CrossRef]
9. Supponen, O.; Kobel, P.; Farhat, M. Video: The inner world of a collapsing bubble. In Proceedings of the 67th Annual Meeting of the APS Division of Fluid Dynamics, San Francisco, CA, USA, 23–25 November 2014.
10. Wenguang, L.; Zhibin, Y.; Sambhaji, K. An improved cavitation model with thermodynamic effect and multiple cavitation regimes. *Int. J. Heat Mass Transf.* **2023**, *205*, 123854.

11. Mingming, G.; Chuanyu, S.; Guangjian, Z.; Coutier-Delgosha, C.; Fan, D. Combined suppression effects on hydrodynamic cavitation performance in Venturi-type reactor for process intensification. *Ultrason. Sonochem.* **2022**, *86*, 106035.
12. Alexander, K.; Anna, Y.; Artur, B. Plug flow of immiscible liquids with low viscosity ratio in serpentine microchannels. *Chem. Eng. J.* **2021**, *417*, 127933.
13. Der, O.; Bertola, V. An experimental investigation of oil-water flow in a serpentine channel. *Int. J. Multiph. Flow* **2020**, *129*, 103327. [CrossRef]
14. Blake, J.R.; Taib, B.B.; Doherty, G. Transient cavities near boundaries. Part 1. Rigid boundary. *J. Fluid Mech.* **1986**, *170*, 479–497. [CrossRef]
15. Blake, J.R.; Gibson, D.C. Cavitation bubbles near boundaries. *Annu. Rev. Fluid Mech.* **1987**, *19*, 99–123. [CrossRef]
16. Lauterborn, W.; Ohl, C.-D. The Peculiar Dynamics of Cavitation Bubbles. *Appl. Sci. Res.* **1998**, *58*, 63–76. [CrossRef]
17. Sagar, J.H.; Moctar, E.O. Dynamics of a cavitation bubble near a solid surface and the induced damage. *J. Fluids Struct.* **2019**, *92*, 102799. [CrossRef]
18. Gibson, D.C.; Blake, J.R. The growth and collapse of bubbles near deformable surfaces. *Appl. Sci. Res.* **1982**, *38*, 215–224. [CrossRef]
19. Blake, J.R.; Cerone, P. A note on the impulse due to a vapor bubble near a boundary. *Anziam J.* **1982**, *23*, 383–393.
20. Brujan, E.A.; Nahen, K.; Schmidt, P.; Vogel, A. Dynamics of laser-induced cavitation bubbles near an elastic boundary used as a tissue phantom. *Am. Inst. Phys.* **2000**, *433*, 251–281.
21. Brujan, E.A.; Nahen, K.; Schmidt, P.; Vogel, A. Dynamics of laser-induced cavitation bubbles near elastic boundaries: Influence of the elastic modulus. *J. Fluid Mech.* **2001**, *433*, 283–314. [CrossRef]
22. Ma, X.; Huang, B.; Zhao, X.; Wang, Y.; Chang, Q.; Qiu, S.; Fu, X.; Wang, G. Comparisons of spark-charge bubble dynamics near the elastic and rigid boundaries. *Ultrason. Sonochem.* **2018**, *43*, 80–90. [CrossRef]
23. Yoshiyuki, T.; Peters, R.I. Bubble collapse and jet formation in corner geometries. *Phys. Rev. Fluids* **2018**, *3*, 081601.
24. Shi-min, L.; Pu, C.; Shuai, Z.; Peng, Y. Experimental and Numerical Study on the Bubble Dynamics near Two-Connected Walls with An Obtuse Angle. *China Ocean Eng.* **2020**, *34*, 828–839.
25. Van-Tu, N.; Thanh-Hoang, P.; Trong-Nguyen, D.; Kim, D.H.; Park, W. Modeling of the bubble collapse with water jets and pressure loads using a geometrical volume of fluid-based simulation method. *Int. J. Multiph. Flow* **2022**, *152*, 104103.
26. Wu, W.; Liu, M.; Zhang, A.-M.; Liu, Y.-L. Fully coupled model for simulating highly nonlinear dynamic behaviors of a bubble near an elastic-plastic thin-walled plate. *Phys. Rev. Fluids* **2021**, *6*, 013605. [CrossRef]
27. Zhao, T.; Zhao, X.; Ma, X.; Huang, B. Numerical investigations of the bubble collapse near an elastic plate. *J. Fluids Struct.* **2021**, *106*, 103372. [CrossRef]
28. Yu, Q.; Xu, Z.; Zhao, J.; Zhang, M.; Ma, X. PIV-Based Acoustic Pressure Measurements of a Single Bubble near the Elastic Boundary. *Micromachines* **2020**, *11*, 637. [CrossRef]